ADVANCED ENERGY MATERIALS
www.advenergymat.de

Decoupling Electron- and Phase-Transfer Processes to Enhance Electrochemical Nitrate-to-Ammonia Conversion by Blending Hydrophobic PTFE Nanoparticles within the Electrocatalyst Layer

*Jianan Gao, Qingquan Ma, Joshua Young, John C. Crittenden, and Wen Zhang**

Electrochemical upcycling of nitrate into ammonia at ambient conditions offers a sustainable synthesis pathway that can complement the current industrial NH_3 production from the Haber–Bosch process. One of the key rate-limiting steps is the effective desorption of gaseous or interfacial bubble products, mainly NH_3 with some minor side products of nitrogen and hydrogen, from the electrode surfaces to sustain available sites for the NO_3^- reduction reaction. To facilitate the gaseous product desorption from the catalytic sites, hydrophobic polytetrafluoroethylene (PTFE) nanoparticles are blended within a CuO catalyst layer, which is shown to eliminate the undesirable accumulation and blockage of electrode surfaces and largely decouples the electron- and phase-transfer processes. The NH_3 partial current density normalized by the electrochemically active surface area (ECSA) increases by nearly a factor of 17.8 from 11.4 ± 0.1 to 203.3 ± 1.8 mA cm^{-2}_{ECSA}. The DFT and ab-initio molecular dynamics simulations suggest that the hydrophobic PTFE nanoparticles may serve as segregated islands to enhance the spillover and transport the gaseous products from electrocatalysts to the PTFE. Thus, a higher ammonia transfer is achieved for the mixed PTFE/CuO electrocatalyst. This new and simple strategy is expected to act as inspiration for future electrochemical gas-evolving electrode design.

1. Introduction

Electrochemical ammonia synthesis from nitrogen gas and nitrate is a sustainable and environmentally benign strategy that could potentially reduce the reliance on the traditional fossil-fuel-based Haber–Bosch NH_3 production.[1] From a thermodynamic point of view, the electrochemical nitrogen reduction reaction (NRR) may benefit from a higher energy efficiency by about 20% than the Haber–Bosch process.[2] Nevertheless, achieving high-efficiency NRR is challenging due to the high dissociation energy of the N≡N bond (941 kJ mol^{-1}) in N_2 and the low standard reduction potential ($E°$) of NRR (0.09 V vs RHE). As a result, the hydrogen evolution reaction (0 V vs RHE) becomes one of the competing reactions.[3] Thus, NRR usually suffers the low Faradaic efficiency for NH_3 generation (mostly <10%) and the low NH_3 production rate as indicate by the low NH_3 partial current density (mostly <1 mA cm^{-2}).[4]

In contrast to N_2, NO_3^- can be disintegrated into deoxygenated species and exhibits a relatively low dissociation energy of the N=O bond (204 kJ mol^{-1}) and positive reaction potential (1.20 V vs RHE).[5] Thus, electrochemical nitrate reduction reaction (NO_3RR) could proceed under ambient conditions and achieve greater reaction kinetics for NH_3 production than NRR.[5b,6] Various catalysts such as CuO, single-atom Fe, CuCl (111)/rutile TiO_2 (110) interface, defective Au_1Cu (111) single-atom alloys, Ru nanoclusters, CuNi alloy, and 3,4,9,10-perylenetetracarboxylic dianhydride (PTCDA) modified Cu have been studied for the electrochemical generation of NH_3 from NO_3^-.[5,6,7] Most relevant studies investigated the electronic structures and interfacial geometry of these electrocatalysts.[5,6,8] Besides the intrinsic properties of the catalysts, the NO_3RR performance also strongly depends on the microenvironment such as the catalyst/water interface, where active reaction sites and transport behavior of gaseous products govern the reaction kinetics and throughput. In this regard, most NO_3RR studies reported the enhanced nitrate adsorption, binding, and hydrogenation via proton-coupled 8 electron transfer steps.[9] However, there is limited knowledge about the desorption of gaseous products, mainly NH_3 with some minor side products of nitrogen (N_2) and hydrogen, from the

J. Gao, Q. Ma, W. Zhang
Department of Civil and Environmental Engineering
New Jersey Institute of Technology
Newark, NJ 07102, USA
E-mail: wzhang81@njit.edu
J. Young, W. Zhang
Department of Chemical & Materials Engineering
New Jersey Institute of Technology
Newark, NJ 07102, USA
J. C. Crittenden
Department of Civil and Environmental Engineering
Georgia Institute of Technology
Atlanta, GA, USA
The ORCID identification number(s) for the author(s) of this article can be found under https://doi.org/10.1002/aenm.202203891.

DOI: 10.1002/aenm.202203891

catalyst sites. Our previous study indicated that owing to the cathodic reactions, the local or interfacial pH could exceed over 12 and NH_3 may stay as a gaseous form at 100%.[10] These gaseous products, such as gas microbubbles, could accumulate and block the active sites, which reduce the available electrocatalyst reaction sites and nitrate-ammonia conversion efficiency.[11]

Recently, gas-diffusion electrodes (GDEs), which usually consist of a porous hydrophobic gas diffusion layer (consist of a carbon fiber substrate and a microporous middle layer) and a catalyst top layer,[12] have proven useful in increasing the local N_2 and CO_2 concentrations by 10–100 times within the catalyst layer and thus improve NRR and CO_2 reduction reaction (CO_2RR).[13] Similar to NRR and CO_2RR (gas reactant delivery involved), NO_3RR also requires effective reactant supply and gaseous product extraction.[14] The three-phase interface design of common GDE couples electron- and phase-transfer and possibly improves the separation of NH_3 and H_2 products from the catalyst layer to gas diffusion layer. Nevertheless, the electrocatalyst layer is usually within 1–10 micrometers in thickness, the produced gaseous products could likely accumulate within the catalyst layer and block the active sites. In general, gas bubbles spontaneously approach hydrophobic particles, forming a three-phase contact interface.[15] Moreover, these bubbles tend to be pinned to hydrophobic surfaces or nucleate at the electrocatalyst when the catalyst layer exhibits hydrophilic/hydrophobic gradient or similar wetting properties.[16] Thus, it is possible to separate the gaseous products from the active sites of electrocatalyst by controlling the hydrophilic and hydrophobic components within the catalyst layer.

This study presents a novel approach to regulate the local gas-liquid microenvironment within the catalyst layer by blending hydrophobic polytetrafluoroethylene (PTFE) nanoparticles into the electrocatalyst layer (CuO nanoparticles) to decouple the electron- and phase-transfer processes and improve spillover and transport of gaseous products from the catalytic sites. Commercial CuO nanoparticles were selected as a model electrocatalyst as they have been commonly used in NO_3RR. PTFE nanoparticles in the catalyst layer are expected to serve as dispersed hydrophobic "islands" that dynamically capture and store gaseous products (NH_3, N_2, and H_2) from the neighboring active sites of CuO nanoparticles. This composite catalyst was deposited onto a commercial GDE substrate (AvCarb GDS2230, Fuel Cell Store, USA) to further regulate the migratory direction of the gas/bubbles, eliminating the bubble induced third phase sandwiched between the cathode and the solution. Atomic force microscopy–scanning electrochemical microscopy (AFM/SECM), density functional theory (DFT) calculations, ab-initio molecular dynamics (AIMD), and electrochemical quartz crystal microbalance (eQCM) were used to reveal and analyze the mechanisms of transfer processes the gaseous molecules of NH_3 and H_2 from the catalyst surface onto PTFE nanoparticles. This novel regulation of the gas–liquid microenvironment provides critical insights into the triple-phase interface of electrocatalysts in NO_3RR.

2. Results and Discussions

2.1. Characterization of CuO Electrocatalysts and the Mixed PTFE/CuO Electrocatalyst on GDE as Cathodes

Figure S1a in the Supporting Information shows the morphology of CuO in a typical SEM image where the grain diameter is 161.3 ± 19.9 nm, which is in agreement with the particle size distribution diagram in Figure S1b (Supporting Information) obtained from DLS. The X-ray powder diffractometer (XRD) pattern Figure S1c (Supporting Information) reveals two strong peaks at 35.51° and 38.74° that correspond to the same facet (111) of CuO.[17] The XPS spectrum in Figure S1d (Supporting Information) further indicates four major peaks of copper. The peaks located at 933.1 and 953.0 eV in the Cu 2p3/2 and Cu 2p1/2 region are attributed to Cu^{2+}, suggesting Cu^{2+} accounted for the vast majority in the commercial copper sample.[18]

Two types of cathodes (namely, CuO/C GDE and PTFE-CuO/C GDE, respectively) were further prepared using the basic catalyst ink (CuO nanoparticles and carbon black) with/without blending PTFE nanoparticles to deposit on the gas diffusion electrode (GDE) substrate. The CuO/PTFE nanoparticles with a specific surface area ratio of PTFE:CuO nanoparticles of 2.5 were selected as an example for the following characterization because this ratio led to the best NO_3RR performance. Figure S2a (Supporting Information) shows the surface coating layer of the mixed CuO/PTFE nanoparticles that were deposited onto the surface of a GDE substrate. The energy-dispersive X-ray spectroscopy (EDS) elemental mapping in Figure S2b–d (Supporting Information) confirms the uniform mixing of CuO, PTFE, and carbon black nanoparticles as indicated by the presence of carbon, copper, and fluoride elements. **Figure 1**a,b compares the structures of the CuO/C GDE and PTFE-CuO/C GDE. The enlarged view shows the triple-phase interface for the in situ capture and storage of gaseous products. Due to the accumulation of gaseous products on CuO electrocatalysts, Figure 1a shows that CuO electrocatalysts without PTFE could be blocked by the in situ generated gas bubbles and block the ion-conducting pathways. The addition of PTFE nanoparticles is expected to attract those gaseous products away from CuO catalyst and increase the electrocatalyst surface for reactions as illustrated in Figure 1b. Figure 1c–d and Figure S3 (Supporting Information) shows the cross-sectional SEM images and top-view SEM images of the two cathodes, respectively. The SEM images indicate that the catalyst layers of the two electrodes were very similar, and the PTFE nanoparticles had no apparent influences on the morphology of the catalyst.

To enhance the transport of nitrate to the inner catalyst layer, another TiO_2 layer was coated on both electrodes that had increased surface hydrophilicity. The water contact angle measurements were performed on the surfaces for four conditions (Figure S4, Supporting Information). The water contact angle for the PTFE-CuO/C electrode without TiO_2 out-layer was ≈145°, indicative of a superior hydrophobicity over that of the CuO/C electrode without TiO_2 (≈115°). After the coating of TiO_2 on top of the electrocatalyst layer, the water contact angles of the CuO/C and PTFE-CuO/C electrodes were reduced to ≈75° and ≈85°, respectively, confirming the different hydrophobicity and hydrophilic properties of the PTFE and TiO_2 particles.

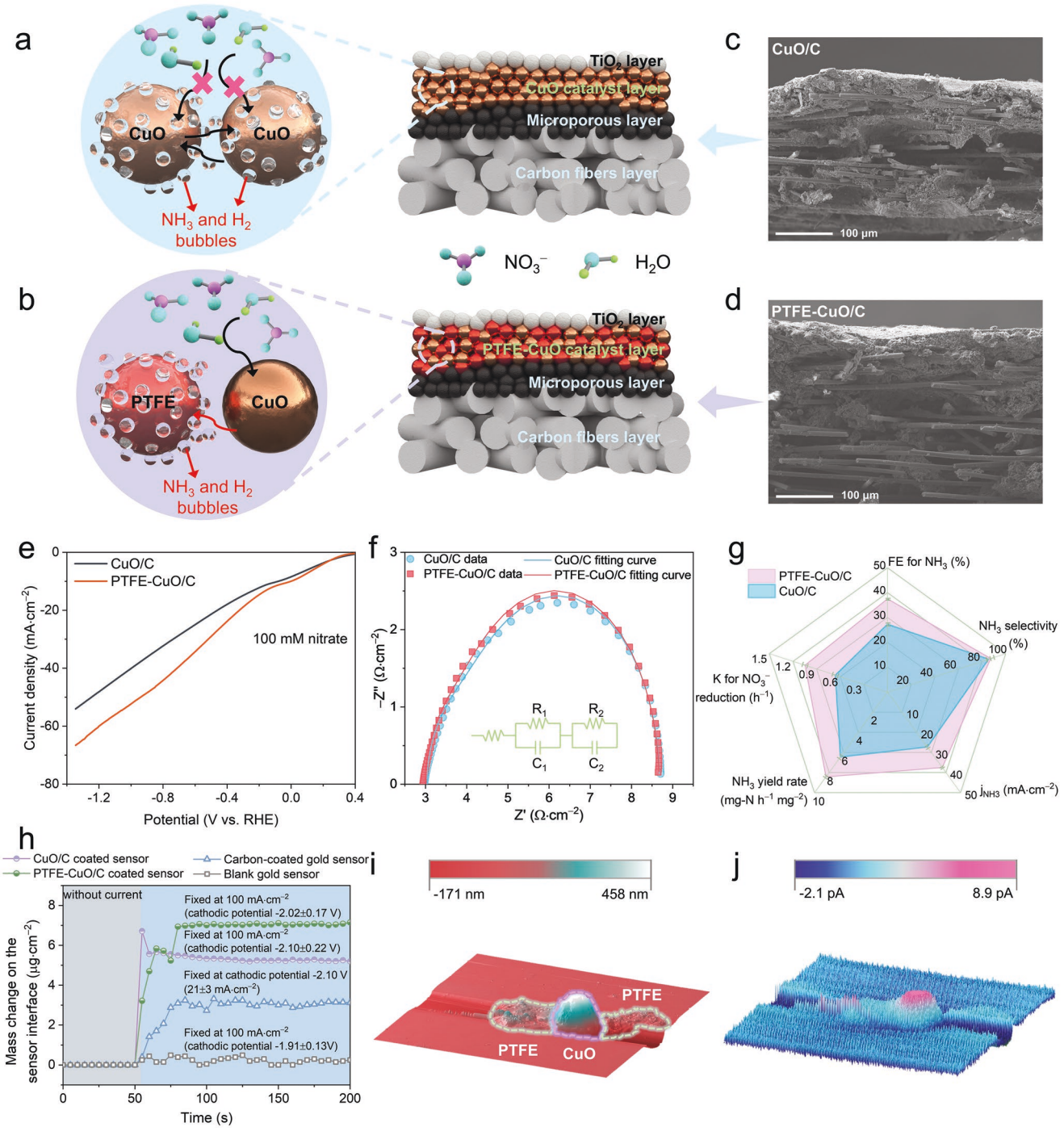

Figure 1. a,b) Illustration of the two different catalyst layers with/without the presence of the blended PTFE nanoparticles in the CuO nanoparticle layer. c,d) Cross-sectional SEM images of PTFE-CuO/C and CuO/C electrodes. e,f) *j*–*V* plots of NO_3^- reduction and Nyquist plots measured at –0.15 V versus RHE of the CuO/C and PTFE-CuO/C electrodes in 0.1 M $NaNO_3$ + 0.5 M Na_2SO_4 electrolyte (pH = 7). g) The comparison of Faradic efficiency (FE) for NH_3, kinetic constant for NO_3^- reduction (*K*), NH_3 yield rate, partial current density (j_{NH3}), and NH_3 selectivity of CuO/C and PTFE-CuO/C electrodes. h) The mass change of coated catalyst layers on the gold sensor and blank gold sensor with/without current or cathodic potential applying in the same aqueous environment (100×10^{-3} M $NaNO_3$ and 0.5 M Na_2SO_4). i,j) AFM/SECM imaging of the mixed PTFE-CuO electrocatalyst.

2.2. Batch Tests of Electrocatalytic Activity and Kinetics

As a measure of the electrocatalytic activity and kinetics of NO_3^-RR in an H-cell (Figure S5, Supporting Information), the LSV data in Figure 1e show that the PTFE-CuO/C electrode exhibited the same onset potential of ≈0.30 V versus RHE (pH = 7) as the CuO/C electrode, indicating that PTFE blends made no changes in the intrinsic catalytic properties of CuO.

However, the PTFE-CuO/C electrode yielded a higher current density with the increase of cathodic potential, indicating a higher reaction activity toward nitrate. Figure 1f shows the Nyquist plots of EIS profiles at the potential of 0.15 V versus RHE (pH = 7). The charge-transfer resistance at the electrode–electrolyte interface (R_1 = 1.15 ± 0.08 and 1.18 ± 0.07 Ω cm^{-2} for CuO/C and PTFE-CuO/C, respectively) and within the inner catalyst layer (R_2 = 0.26 ± 0.07 and 0.24 ± 0.07 Ω cm^{-2} for CuO/C and PTFE-CuO/C, respectively) were derived from the hypothetical equivalent circuit as shown in sect of Figure 1f. R_1 was barely affected because the TiO_2 coating layer was the same out-layer. The similar values R_2 for CuO/C and PTFE-CuO/C indicate the appropriate addition of PTFE nanoparticles did not affect the conductivity inside the catalytic layer.

NO_3^- reduction test was first performed in an H-shaped electrochemical reaction cell (Figure S5, Supporting Information) at a fixed current density (100 mA cm^{-2}). Figure S6 (Supporting Information) shows the product concentration changes over reaction time for the two electrodes. Product analysis in Figure S7 (Supporting Information) indicated that the NO_3^- reduction on CuO catalyst yielded mainly NH_3 with a small amount NO_2^- and N_2. To exclude the effect of TiO_2 on nitrate reduction to ammonia, the ammonia yields from the blank carbon substrate and the TiO_2/C coating were measured (Figure S8, Supporting Information). The total ammonia generation of the blank carbon (0.59 ± 0.04 mg for 1 h) substrate and TiO_2/C (0.40 ± 0.03 mg for 1 h) were far below that of CuO/C (7.74 ± 0.20 mg for 1 h) and PTFE-CuO/C (10.11 ± 0.12 mg for 1 h). This confirms that the difference in ammonia yield on CuO/C and PTFE-CuO/C was primarily attributed to the presence of PTFE particles. Figure 1g is a wind rose graph that illustrates the Faradic efficiency (FE), kinetic constant for NO_3^- reduction (K), NH_3 yield rate, and partial current density (j_{NH3}) for the CuO/C electrode, which were 27.3 ± 0.6%, 0.66 ± 0.03 h^{-1}, 1.9 ± 0.1 mg N h^{-1} mg^{-1}, and 27.3 ± 0.6 mA cm^{-2}, respectively. In comparison, the PTFE-CuO/C electrode exhibited a higher FE of 37.5 ± 0.4%, K of 1.05 ± 0.03 h^{-1}, NH_3 yield rate of 2.5 ± 0.1 mg N h^{-1} mg^{-1}, and j_{NH3} of 37.5 ± 0.4 mA cm^{-2}. However, there was no significant changes in NH_3 selectivity (85.6 ± 1.7% and 87.2 ± 2.9% for the CuO/C and PTFE-CuO/C electrodes, respectively). This improved performance of NO_3^-RR on PTFE-CuO/C supports our above speculation that a timely gas product desorption (mainly NH_3 and H_2) from the active sites (CuO) to the hydrophobic "island" (PTFE nanoparticles) could alleviate the block effect of gaseous products on the ion transport channels and the catalytic sites, rather than changing the intrinsic catalytic properties of the CuO catalyst.

2.3. Interfacial Characterization of Gaseous Product Adsorption on Electrocatalyst

EQCM was employed to sensitively detect the interfacial adsorption of reactants and product generation on the CuO/C and PTFE-CuO/C electrodes.[19] As illustrated in Figure 1h, the thin films coated with CuO/C or PTFE-CuO/C showed similar state baselines in the electrolyte (100 × 10^{-3} M $NaNO_3$ and 0.5 M Na_2SO_4). After applying a negative current density of 100 mA cm^{-2} (the same cathodic current used for NO_3^-RR that corresponded to the required cathodic potential of CuO/C and PTFE-CuO/C films of −2.10 ± 0.22 and −2.02 ± 0.17 V, respectively), the mass of CuO/C and PTFE-CuO/C films dramatically increased and reached a stable level of 5.2 and 7.1 μg cm^{-2}, respectively, due to the cation adsorption and gaseous/bubble product accumulation on the films. To verify if the mass changes were caused by the cation adsorption and the gaseous product accumulation within the catalyst film, the mass changes of the pristine carbon-coated gold sensor (under a cathodic potential of −2.10 V and the current density of 21 ± 3 mA cm^{-2}) and the pristine or uncoated gold sensor (under a cathodic potential of −1.91 ± 0.13 V and the current density of 100 mA cm^{-2}) were monitored. Under the same cathodic potential, the carbon-coated gold sensor rendered a lower response current density than those of CuO/C and PTFE-CuO/C films, which suggests fewer gaseous products (H_2 and NH_3) were generated by the carbon-coated gold surface. The stable mass level of the carbon-coated gold surface was 3.1 μg cm^{-2}, which was also lower than those of CuO/C and PTFE-CuO/C films. The stable mass level of the pure gold sensor was 0.2 μg cm^{-2} due to minimum adsorption of any gaseous products or cations. Thus, the higher mass deposition on the PTFE-CuO/C film should result from the faster adsorption and formation of NH_3 and H_2 with the presence of the dispersed PTFE nanoparticles as the hydrophobic "island."

The AFM/SECM results of the PTFE-CuO mixture in Figure 1i,j reveals the topography and current mapping obtained during the reduction of 5 × 10^{-3} M $[Ru(NH_3)_6]^{3+}$ in 0.1M KCl by sweeping the sample particles using the Pt-coated probe that was at a DC potential of ≈0.3 V versus RHE. The current mapping provide imaging contrast based on feedback mode that measures the Faradaic current of a redox mediator (e.g., $[Ru(NH_3)_6]^{3+/2+}$) reacting with the probe or the sample surface. In our case, the DC biased AFM/SECM probe approached the CuO particles, the surface of CuO particles will be polarized since the CuO particles are conducting. As a result, the redox mediator underwent an enhanced diffusion and reaction with the probe due to the presence of this locally enhanced electric field between the probe and the CuO particles, which caused an increase in the tip current and thus the current mapping contrast. On the contrary, when this DC biased AFM/SECM probe was brought into close proximity with the insulating PTFE particles, negative feedback occurred as the diffusion of the redox mediator to the probe was interfered by the inert properties of the PTFE nanoparticles. This results in a lower concentration of redox mediator measured by the probe, and therefore a lower current density. In accordance with our initial hypothesis, we found a feedback enhancement on top of the CuO particles at a resolution of ≈2 μm. The AFM/SECM mapping current difference between CuO and PTFE islands under a given tip voltage (≈0.3 V vs RHE) is about 11 pA. The difference in mapping current strength confirmed the decoupling of electron transfer process, which means CuO nanoparticles provide "active" reaction sites during the electrocatalytic process. The PTFE nanoparticles served as local hydrophobic centers to

facilitate the desorption and transfer of the gaseous products from NO_3RR.[10a]

2.4. Regulation of Gaseous Products Migration Direction within the Catalyst Layer

To further investigate the transfer of gaseous products from the electrocatalyst and the PTFE "islands" to the cathodic electrolyte, we evaluated the NO_3RR in an electrolysis flow cell by circulating 1 M H_2SO_4 to the carbon fibers layer side of GDE to enhance the membrane transfer of NH_3 from the catalyst layer (**Figure 2**a), which produced $(NH_4)_2SO_4$ in the trap or draw solution. Figure S9 in the Supporting Information compared the nitrogen species evolution in the flow-cell with the two different electrocatalysts coated on GDE as cathodes. Figure 2b shows that all electrical efficiency indicators related to NO_3RR of PTFE-CuO/C GDE outperformed CuO/C GDE and all increased compared to the results in Figure 1g. Specifically, the partial current density for NH_3 production on the CuO/C and PTFE-CuO/C GDEs increased to 33.8 ± 0.1 and 46.0 ± 1.0 mA cm^{-2}, respectively, suggesting that timely extraction of gaseous products from the active sites could accelerate the NO_3RR performance. Besides, the ratio of the recovered NH_3 in the H_2SO_4 trap tank to the total generated NH_3 for PTFE-CuO/C (89.5 ± 0.2%) fabricated flow-cell was higher than that of CuO/C GDE equipped flow-cell (75.0 ± 1.4%). This further confirms the roles of the blended

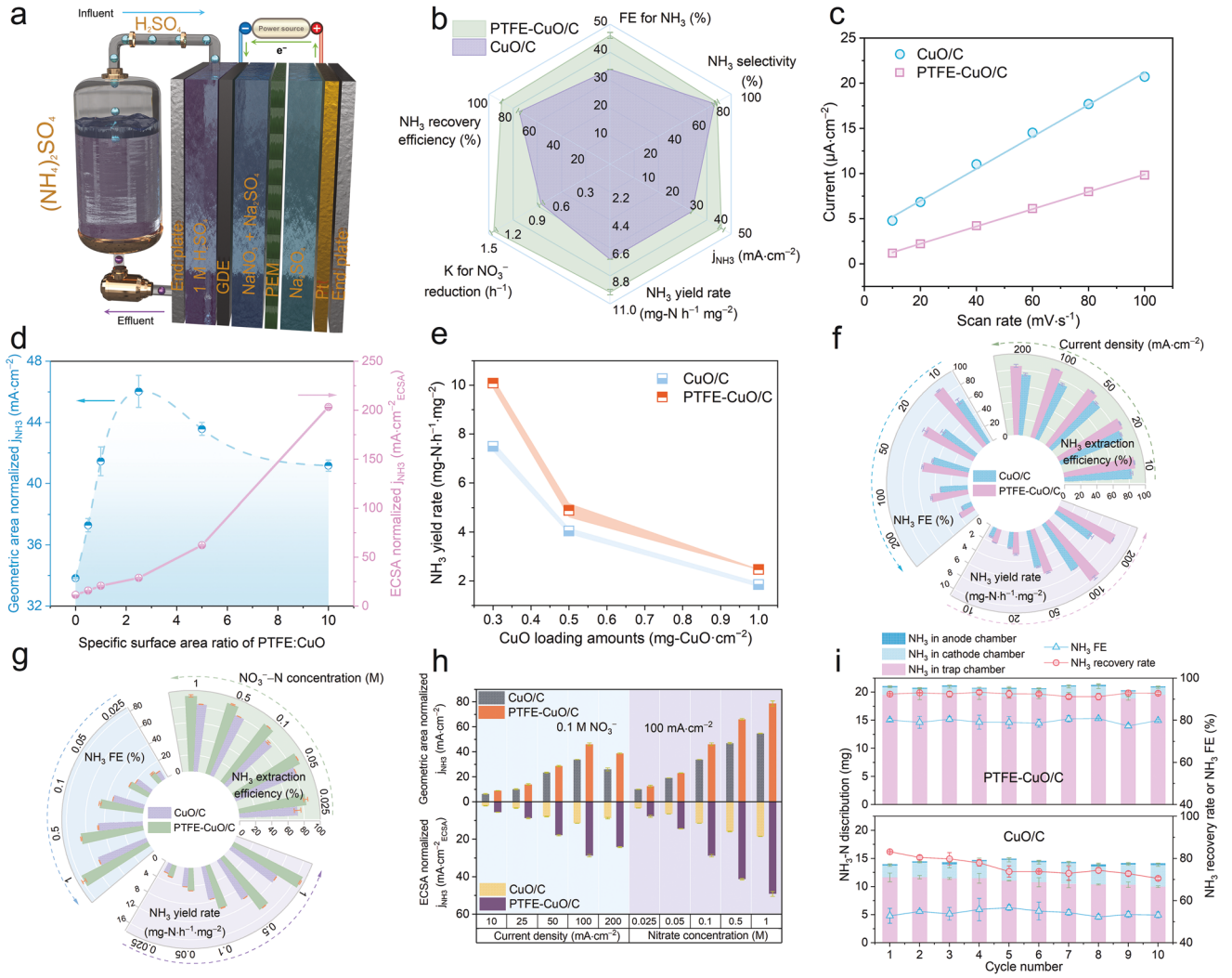

Figure 2. NO_3RR performance in a flow cell. a) Illustration of the flow-cell used for NO_3RR experiments and in-situ NH_3 extraction. b) The comparison of Faradic efficiency (FE) for NH_3, kinetic constant for NO_3^- reduction (K), NH_3 yield rate, partial current density (j_{NH3}), NH_3 recovery efficiency, and NH_3 selectivity of CuO/C and PTFE-CuO/C electrocatalysts. c) The calculation of C_{dl} based on the current values (I_a and I_c) and the scan rate. d) The comparison of geometric area normalized and ECSA normalized j_{NH3} with different specific surface area ratio of PTFE:Cu. e) The NH_3 yield rate with different CuO loading amounts. f,g) The comparisons of NH_3 extraction efficiency, NH_3 FE, and NH_3 yield rate under various current densities and initial NO_3^-–N concentrations respectively. h) The comparison of geometric area normalized and ECSA normalized j_{NH3} with different current densities and NO_3^-–N concentrations. i) Stability test of the CuO/C and PTFE-CuO/C electrocatalysts at a constant current density of 100 mA cm^{-2}. The electrolyte was replaced by a new solution of 100×10^{-3} M $NaNO_3$ + 0.5 M Na_2SO_4 for each cycle.

PTFE nanoparticles in promoting gaseous products extraction from the catalyst layer.

2.5. Optimization of the Blending Ratio of PTFE into CuO/C Electrocatalyst and Catalyst Loading Amount

Excessive amounts of PTFE could trap gases products, influence potentially the electrical, electrolyte, and proton accessibility of the catalyst sites for NO_3^- reduction, and thus reduce the contact between the electrode and electrolyte.[13b,20] To verify this issue, we measured the electrochemically active surface area (ECSA) for the electrocatalysts with different blend ratios of PTFE. Figure S10 (Supporting Information) shows the CV curves performed on GDEs with different surface area ratios of PTFE:CuO nanoparticles from 0 to 10, and the calculated C_{dl} based on the current values (I_a and I_c) and the scan rate. The ECSA of PTFE:CuO specific surface area ratio of 0, 0.5, 2.5, and 10 were 11.8, 9.4, 6.4, and 0.8 cm^2_{ECSA}, respectively. Figure 2c shows that the ECSA decreased after adding PTFE owing to the less contact with the electrolyte. According to the calculation of ECSA, at the same loading amounts of carbon black and CuO, the ECSA of PTFE-CuO(2.5)/C decreased by 45% as compared to the CuO/C electrocatalyst. However, the ECSA-normalized partial current density for NH_3 production on PTFE-CuO/C significantly increased to 28.8 ± 0.7 mA cm^{-2}_{ECSA}, about 2.5-fold of that CuO/C (11.4 ± 0.1 mA cm^{-2}_{ECSA}). Further considering the 1.4-fold increased geometric area normalized j_{NH3}, though there is a loss of the active reaction sites, the activity of NO_3^- reduction to NH_3 was still significantly improved by blending PTFE nanoparticle "islands" within the catalyst layer that helped decouple the electron and phase transform.

Based on the experimental data of nitrogen species evolution in Figure S11 (Supporting Information), the ECSA-normalized j_{NH3} (Figure 2d) shows that as the specific surface area ratio of PTFE:CuO increased, the ECSA-normalized j_{NH3} increased and reached the highest level (203.3 ± 1.8 mA cm^{-2}_{ECSA}) at PTFE:CuO specific surface area ratio of 10. However, the geometric area normalized j_{NH3} followed a volcano-shaped trend with a maximum value obtained at PTFE:CuO specific surface area ratio of 2.5 (46.0 ± 1.0 mA cm^{-2}). Moderate amount of PTFE islands can capture and storage the gaseous products inside the catalyst layer. Nevertheless, excess PTFE nanoparticles will lower the electrical conductivity, electrolyte and protons accessibility for NO_3^- reduction, leading to the decrease of Faradic efficiency for NH_3.[21]

To verify the feasibility of this strategy for different catalyst loading mass, six CuO/C and PTFE/CuO/C with different CuO loading amounts (0.3, 0.5, and 1.0 mg-(CuO) cm^{-2}) and the same PTFE:CuO specific surface area ratio (2.5) were fabricated. The detailed experimental results of nitrogen species concentrations were shown in Figure S12 in the Supporting Information. As illustrated in Figure 2e, the yield rate for NH_3 decreased with increasing the CuO loading amount and all increased when introducing PTFE nanoparticles into the catalytic layer. This could be attributed to the limited solid-liquid interface exposed to NO_3^- ions. Simply increasing the CuO loading mass leads to dead reaction zone and gains no benefits for NO_3^- reduction.

2.6. Investigation of the Effects of Current Density and Nitrate Concentration on Nitrate Reduction and NH_3 Distribution

Figures S13 and S14 (Supporting Information) shows the time-resolved nitrogen species concentrations for the two electrocatalysts under different current densities and initial NO_3^- concentrations. Figure 2f,g shows within a wide range of the current density (10 to 200 mA cm^{-2}) or the NO_3^- concentration (0.025–1 M), PTFE-CuO/C achieved greater levels of FE, the NH_3 yield rate, and the NH_3 recovery rate than CuO/C. Notably, the NH_3 yield rates under 200 mA cm^{-2} of PTFE-CuO/C and CuO/C were both lower than that under 100 mA cm^{-2}. This is because higher current densities correspond to higher negative cathodic potential that will trigger hydrogen evolution via Tafel or Heyrovsky routes as evidenced by the intensive surface bubbling on the cathode surface.[22] Thus, more electrical energy was consumed or wasted on hydrogen production rather than ammonia production. Figure 2h further reveals that the partial current density (j_{NH3}) increased with the applied current density. Moreover, the ECSA normalized j_{NH3} of PTFE-CuO/C were ≈2.8 and 2.7 times that of CuO/C, respectively when applying the current density of 200 mA cm^{-2} or 1 M NO_3^-. This again confirms the contribution of the blended the PTFE nanoparticles to the NO_3^- reduction as mentioned previously by effectively diverting the produced NH_3 from CuO/C electrocatalyst. Furthermore, Figure 2i shows the stability tests of CuO/C and PTFE-CuO/C electrodes. The PTFE-CuO/C electrode can consistently produce NH_3 for 10 continuous cycles (10 h in total) without appreciable degradation in capacity, Faradaic efficiency, and recovery efficiency of NH_3. The NH_3 recovery efficiency of CuO/C electrode slightly dropped from 83.2% to 70.5% after 10 continuous cycles. This could be attributed to the low wetting resistance of CuO/C catalyst without the presence of PTFE.[23] The strategy of introducing PTFE nanoparticles into the catalyst to enhance the NO^{3-} reduction activity is thus important for improving the stability of the electrocatalyst.

According to previous studies,[10b,24] CuO may undergo a valence shift and form mixed-valence states of Cu (Cu^0, Cu^{1+}, and Cu^{2+}) under electrochemical reactions. Our data in Figure S15 (Supporting Information) shows that after 1 h of electrolysis under –100 mA cm^{-2} cathodic current, the surface Cu^{2+} species ratio of CuO/C and PTFE-CuO/C all decreased and reached stable levels of 59.7 ± 4.3% and 61.1 ± 3.9%, respectively, due to the increase of Cu^{0+} and Cu^{1+} species. Thus, the presence of PTFE did not significantly change the valence shift of CuO. Besides, the morphology of PTFE-CuO/C is not significantly changed after 10 h of electrolysis under –100 mA cm^{-2} cathodic current (Figure S16, Supporting Information).

2.7. Mechanistic Analysis of Performance Improvement

The catalyst microenvironment and reaction interfaces are important for NO_3RR and subsequent NH_3 extraction from the electrolyte. For the traditional catalyst layer design with a single active component (e.g., CuO/C), the nitrate reduction to ammonia involves 8 electrons transfer (electron-transfer process) and gaseous products transfer (phase-transfer process) that occur simultaneously on the electrocatalyst. The

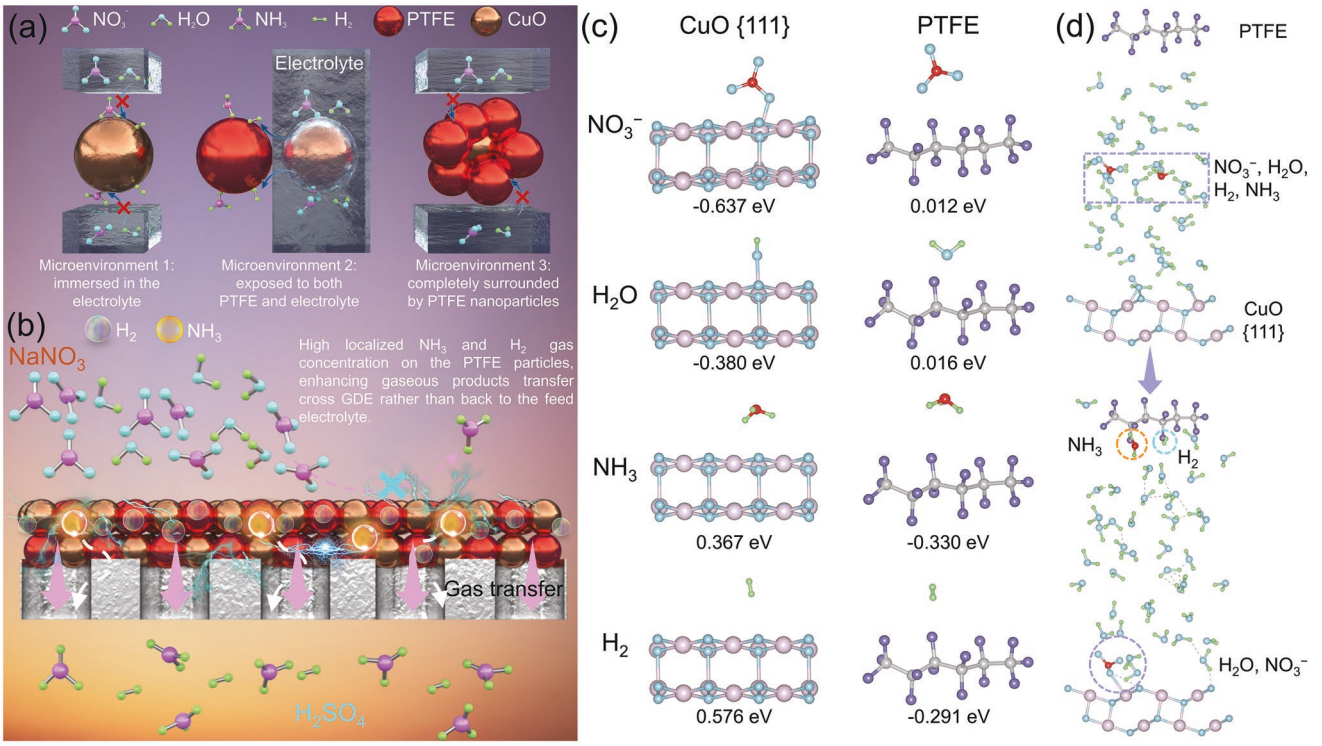

Figure 3. a) Three possible microenvironments of CuO electrocatalyst. b) Illustration of the gaseous products mass transport inside the catalyst layer with PTFE adding. c) Free energy of NO_3^-, H_2O, NH_3, and H_2 on Cu (111) and PTFE. d) Ab initio molecular dynamics (AIMD) simulation of the molecular migration of NO_3^-, H_2O, NH_3, and H_2 on CuO (111) and PTFE.

gaseous products on the electrocatalyst could block the nitrate ion-conducting pathways and reduce the catalyst activity. After blending the hydrophobic "island" (PTFE) with the active component (CuO), the generated bubbles tend to be pinned to the PTFE surfaces via hydrophobic interaction rather than nucleation on CuO.[16] Thus, the decoupling of the electron- and phase-transfer processes could facilitate the mass transfer of the gaseous products and promote electrocatalytic reactions.

Figure 3a illustrates three possible microenvironments of the PTFE-CuO/C catalyst layer in which the CuO electrocatalysts were (1) immersed in the electrolyte; (2) exposed to both PTFE and electrolyte; and (3) completely surrounded by PTFE nanoparticles. In the first situation, the active sites of CuO are often blocked by the generated gaseous products. In the third situation, CuO (bronze ball) is blocked by excessive PTFE nanoparticles (red balls) and thus no longer active toward NO_3RR. Only the second situation yields an ideal three-phase interface, where the gaseous products are effectively extracted from the hydrophilic CuO nanoparticles and transferred to the hydrophobic PTFE nanoparticles.[15] This transfer process enables the interaction of NO_3^- molecules and protons to the active sites. Figure 3b shows the high gas concentrations of NH_3 and H_2 on PTFE nanoparticles enhanced their migration from the inner catalyst layer cross microporous layer to the carbon fiber layer.[11]

Furthermore, DFT simulations were performed to analyze the preferential adsorption of NO_3^- and H_2O on CuO sites and subsequent desorption of NH_3 and H_2 to the PTFE. The (111) facet of CuO was also chosen based on the exposed lattice analysis of the CuO. A typical PTFE long-chain structure was chosen as the model for PTFE.[25] Figure 3c shows the different molecular interactions on CuO and PTFE surfaces. NO_3^-, H_2O, NH_3, and H_2 were adsorbed on the CuO (111) surface and PTFE structure in different orientations until the lowest energy configuration was found, and the free energy was then computed for each. The free energy of NO_3^- and H_2O on CuO (111) were –0.637 and –0.380 eV, which are more negative than those on PTFE. Conversely, PTFE exhibited lower adsorption energies (–0.330 and –0.291 eV) for NH_3 and H_2 than CuO (111). The results suggest that NO_3^-/H_2O and NH_3/H_2 pairs preferentially adsorb on CuO (111) and PTFE, respectively.

AIMD simulations further delineate the molecular migration of NO_3^-, H_2O, NH_3, and H_2 on the surfaces of CuO (111) and PTFE. AIMD follows the trajectories of all atoms while computing interatomic interactions quantum mechanically based on the Hellmann–Feynman theorem and can therefore describe chemical reactions and molecular interactions accurately. As an example, Paolucci et al. performed AIMD simulations to visualize the diffusion trajectories of $[Cu^+(NH_3)_2]^+$ and $[Cu^{2+}(NH_3)_4]^{2+}$ species in chabazite cages and confirmed that both NH_3-ligated species are mobile enough to allow Cu to move away from the equilibrium position.[26] Two simulation cells containing a CuO/PTFE interface, with both surfaces exposed to H_2O (40 molecules of H_2O were included), were created; each cell differed in the reactants and products that were included and their position. First, NO_3^-, H_2, and NH_3 were placed in the middle of the simulation cell (equidistant from both the CuO and PTFE surface), and a 1000 ps trajectory was

performed. Figure 3d shows that after this time, the reactant (NO_3^-) and proton source (H_2O) tend to transfer to the hydrophilic active sites of CuO (111), and the gaseous products (NH_3 and H_2) prefer to migrate to hydrophobic sites (PTFE). This finding agrees with the trends found in the DFT-computed adsorption energies of these species on CuO and PTFE. Moreover, another MD study also suggested the hydrophobic surface (e.g., PTFE particles) could also enhance the transfer of the surface-generated nanobubbles of NH_3 or H_2 from hydrophobic electrode (e.g., CuO) and result in surface pinning to PTFE particles.[16]

A second simulation cell containing H_2 and NH_3 molecules placed in the middle of the simulation cell (equidistant from both the CuO and PTFE surfaces), and 1000 ps trajectory was performed as same with as a first simulation. After this simulation, the NH_3 and H_2 prefer to migrate to hydrophobic sites (PTFE) as shown in Figure S17 (Supporting Information), whereas the H_2O molecules tend to transfer and bind to the hydrophilic active sites of CuO (111).

3. Conclusion

This work developed a novel electrocatalyst layer design by introducing PTFE nanoparticles into the CuO catalyst layer on the gas diffusion electrode surface. The PTFE nanoparticles act as "islands" at the triple-phase interface that facilitate the in situ capture and storage of gaseous products, and thus eliminate the blockage of gaseous products for the ion-conducting pathways and electrocatalyst surface. Using the resultant PTFE-CuO/C GDE, the electrochemically active surface area (ECSA) normalized NH_3 partial current density increased by nearly a factor of 17.7 that of electrode without PTFE. The PTFE-CuO/C GDE shows an all-round improvement of Faradic efficiency for NH_3 production, kinetic constant for NO_3^- reduction, NH_3 yield rate, NH_3 partial current density, and NH_3 recovery efficiency than that of CuO/C GDE. Interestingly, the NH_3 selectivity of CuO/C GDE (85.6 ± 1.7%) and PTFE-CuO/C GDE (87.2 ± 2.9%) were similar, confirming the improved NO_3RR performance was attributed to the timely gas product desorption from the active sites (CuO) to the hydrophobic "island," rather than changing the intrinsic catalytic properties of the catalytic material. DFT calculations, EQCM, and AFM/SECM unraveled the spontaneous migration of gaseous products from CuO to PTFE, the mass changes within the catalyst layer caused by bubble generation and storage, and the electrical response differences on CuO and PTFE, confirming the decoupling of electron- and phase-transfer within the catalyst layer. This work presents a general strategy for NO_3RR electrode design, which could also expand to other electrochemical gas-evolving electrode design.

4. Experimental Section

Preparation of Gas Diffusion Electrodes with Different Inner Catalyst Layer: The CuO-coated gas-diffusion electrode (GDE) was prepared by air-brush painting of the catalyst ink. Briefly, 5 mg of Vulcan XC 72 carbon black (Fuel Cell Store) and 10 mg of CuO nanoparticles (Thermo Scientific, APS 30–200 nm) were dispersed in 2 mL isopropanol. Then, different amounts (0, 3.9, 7.7, 19.1, 38.5, and 76.5 mg) of PTFE nanoparticles (Nanoshel LLC, APS 30–50 nm) were dispersed in 4 mL isopropanol, respectively. After sonication for 1 h, the above two suspensions were mixed with 50 µL Nafion solution (D521 Nafion Dispersion at 5 wt%, containing ≈2 mg Nafion) and then sonicated for another 1 h. The resulting inks were named as PTFE:CuO(0.0), PTFE:CuO(0.5), PTFE:CuO(1.0), PTFE:CuO(2.5), PTFE:CuO(5.0), and PTFE:CuO(10.0). The values in parentheses represent the specific surface area ratio of PTFE:CuO nanoparticles. A commercial GDE (Fuel Cell Store, AvCarb GDS2230 substrate) was purchased to deposit electrocatalysts and prepare the gas-permeable cathode. This GDE was a carbon fiber paper with two different sides, one with PTFE coating and the other with a microporous layer. The received GDE was further pretreated with 10 wt% PTFE solution on the PTFE coated carbon fiber side to reach a 1 mg cm^{-2} PTFE loading amount. After PTFE coating operation, the GDE was transferred into a muffle furnace and heated to 270 °C for 10 min. The electrocatalyst ink was uniformly sprayed on the PTFE microporous layer side (coating area 2 × 2 cm^2) of this GDE using an airbrush as reported elsewhere.[12] The catalyst loading of CuO nanoparticles was around 0.3 ± 0.03, 0.5 ± 0.05, or 1.0 ± 0.05 mg cm^{-2}. After drying overnight, another catalyst ink made of TiO_2 anhydrous (powder, Thermo Scientific) was further sprayed on top of the obtained electrodes at a coating mass of 0.1 ± 0.02 mg cm^{-2} to obtain a hydrophilic catalytic layer.[27] All the samples were further dried in the air overnight before testing.

Characterization of the Electrocatalysts: The morphology and chemical compositions of PTFE and CuO nanoparticles were analyzed by JSM-7900F field emission scanning electron microscope (FE-SEM) (JEOL, Japan) at 15 kV with coupled EDS. Hydrodynamic particle size of the CuO nanoparticles in water suspension was determined by dynamic light scattering (DLS) on a Malvern Nano-ZS. The crystalline structures were investigated by XRD (Philips, EMPYREAN, PANalytical Almelo) with a Co Ka radiation (λ = 1.789 Å). The surficial chemical states and compositions were measured by X-ray photoelectron spectroscope (XPS, Thermo, K-Alpha, USA) with a monochromatic Al Kα radiation ($h\nu$ = 1486.6 eV). All spectra were calibrated using the binding energy of C 1s (284.8 eV) as a reference.

Electrochemical Measurements: To investigate the electrocatalytic activity and kinetic of NO_3^-RR, Linear sweep voltammetry (LSV), and electrochemical impedance spectroscopy (EIS) tests were performed using a CH Instruments 700E Potentiostat with a typical three-electrode H-type cell, consisting of a proton exchange membrane (Nafion 117, Dupont), a CuO-coated gas-diffusion electrode (GDE), a Pt plate, and Ag/AgCl electrode as working electrode, counter electrode, and reference electrode, respectively. The applied potentials measured against the Ag/AgCl reference electrode in saturated KCl were converted to the reversible hydrogen electrode (RHE) reference

$$E(\text{vs RHE}) = E(\text{vs Ag/AgCl}) + 0.059 \times \text{pH} + 0.197 \quad (1)$$

These electrodes were immersed in 100 × 10^{-3} M $NaNO_3$ and 0.5 M Na_2SO_4 under ambient temperature. LSV polarization curves were performed at a scan rate of 100 mV s^{-1}. According to LSV tests, the onset over-potential (10 mA cm^{-2}) of CuO/C and CuO-PTFE/C electrodes were all located at ≈0.15 V versus RHe (pH = 7), whereas NO_3RR starts to occur. Thus, EIS was conducted at the potential of 0.15 V versus RHE for the CuO/C and PTFE-CuO/C electrodes, under the alternating current (AC) within the frequency range from 10^5 to 10^{-2} Hz at an incremental change of 5 mV.

The electrochemical double-layer capacity (EDLC, C_{dl}) was determined via cyclic voltammetry (CV), which was recorded within a potential range of ± 0.05 V, where only double-layer charging and discharging occur (no Faradaic process) with a scan rate (ν) of 10–100 mV s^{-1}.[28] C_{dl} was calculated by Equation (2) according to the charging current values (I_a and I_c) and was then plotted versus the CV scan rate. The slope of the linear regression gave the double-layer capacitance and regarded as the indicator of active sites number.[29] The electrochemically active surface area (ECSA) for the electrocatalysts was further determined by dividing

the obtained double-layer capacity by the standard electroactive surface area for metal oxide based systems (60 µF cm^{-2})[30]

$$\frac{I_a - I_c}{2} = C_{dl}\nu \quad (2)$$

eQCM and AFM/SECM Measurements: Electrochemical quartz crystal microbalance (eQCM, 10M, GAMRY Instrument), which combines the QCM with a potentiostat (CH Instruments 760E) as shown in Figure S18 (Supporting Information), was employed to measure the interfacial mass changes on a substrate surface (e.g., gold) at an ng cm^{-2} level. A typical three-electrode system was constructed with a gold crystal sensor (5 MHz, GAMRY Instrument), a platinum (Pt) wire, and an Ag/AgCl electrode as working electrode, counter electrode, and reference electrode respectively. The above-obtained catalyst inks with/without PTFE particles were dropped cast on the gold crystal sensor surface and air-dried overnight as illustrated in Figure S19 in the Supporting Information. The catalyst-coated gold sensor substrates were placed in a static cell filled with 100×10^{-3} M $NaNO_3$ and 0.5 M Na_2SO_4. Then, a constant current density (100 mA cm^{-2}), a same level of cathodic current used in NO_3RR experiment, was applied to the gold sensor to enable NO_3RR and the frequency changes were recorded. The frequency data was further analyzed to obtain the mass of the sensors by using the supporting software (Echem Analyst, GAMRY INSTRUMENT) based on the Sauerbrey equation

$$\Delta f = -\frac{2f_0^2}{A\sqrt{\rho_q \mu_q}}\Delta m \quad (3)$$

where Δf is the frequency change (Hz), Δm is the mass change (g), f_0 is the resonant frequency (Hz), A is the piezoelectrically active crystal area (cm^2), ρ_q is the density of quartz (g cm^{-3}), and μ_q is the shear modulus of quartz for AT-cut crystal (g cm^{-1} s^{-2}).[19]

The atomic force microscopy–scanning electrochemical microscopy (AFM/SECM) measurements were performed on the Bruker Dimension Icon equipped with standard PeakForce SECM accessories as detailed elsewhere.[31] Both the probe and the sample are working electrodes sharing the same reference and counter electrodes. Prior to the PeakForce SECM measurement, all PeakForce SECM probes (tip radius of 25 nm and tip height of 215 nm, Bruker Nano Inc, CA, US) were tested by performing a few cyclic voltammetry in a standard three-electrode electrochemical cell with a Pt counter electrode and a standard Ag/AgCl reference electrode (CH Instruments, Inc.). The electrochemical cell was filled with 1.8 mL of 10×10^{-3} M $[Ru(NH_3)_6]Cl_3$ in 0.1 M KCl. A bipotentiostat (CHI700E, CH Instrument) was connected to the electrochemical cell to perform the cyclic voltammetry analyses with a scanning voltage from 0 to –0.4 V versus Ag/AgCl at 50 mV s^{-1} applied to PeakForce SECM probes. The PeakForce SECM scan was performed using an interleaved scan mode with a lift height of typically 40–150 nm between the probe and the sample surface. After verifying SECM standard test sample (silicon nitride pattern cover on the Pt layer) the sample-coated substrate was placed into the same fluidic cell to replace the SECM standard test sample. The same SCEM scanning procedure was performed on the sample surface at a DC bias of –0.3 V applied to the probe at the scan rate of 0.2 Hz and a scan size is 10×10 µm, which caused reduction of $[Ru(NH_3)_6]^{3+}$ to $[Ru(NH_3)_6]^{2+}$ and thus enhanced the tip current and the mapping contrast.

Operation of the Electrochemical Flow Cell: Nitrate reduction experiments were carried out in an electrochemical flow-cell as shown in Figure 2a. The CuO-coated gas-diffusion electrode (GDE) and Pt plate (exposed area: 2 cm × 2 cm) were employed as cathode and anode, respectively. A proton exchange membrane (Nafion 117, Dupont) was used to separate the cathode and anode chambers. 0.5 M Na_2SO_4 with/without $10–1000 \times 10^{-3}$ M $NaNO_3$ solutions were filled into the cathode and anode chambers, respectively. 1 M H_2SO_4 was circulated to the carbon fibers layer side of GDE (trap chamber) to change the gaseous products (NH_3 and H_2) migratory direction and protonate the in situ transferred NH_3 from the catalyst to NH_4^+.

The aqueous concentrations of NO_3^-, NH_3, and NO_2^- were quantified by UV–vis spectrophotometry based on the cadmium reduction method (HACH method 8039), the salicylate method (HACH method 8155), and the diazotization method (HACH method 8507), respectively. The produced NH_3 was carefully controlled to rule out possible contaminations (e.g., NH_3 in the air) based on the previous report.[32] Specifically, 0.3 mL electrolyte sample was taken out during or after the nitrate reduction test and diluted to the detection range for NO_3^-, NH_3, and NO_2^-.

Performance Evaluation of the Electrocatalytic NO_3^- Reduction to NH_3: The Faradic efficiency (FE) (%) and selectivity (%) for NH_3 were calculated by Equations (4) and (5) respectively

$$\mathrm{FE}(\%) = \frac{n \times F \times N_i}{Q} \times 100 \quad (4)$$

$$S_{NH_3}(\%) = \frac{\Delta[NH_3]}{\Delta[NO_3^- - N]} \times 100 \quad (5)$$

where n is the electron transfer number (8) per more of reduced nitrate to NH_3, F is the Faraday constant (96 487 C mol^{-1}), N_i is the amount (mol) of the produced NH_3, Q is the total charge (C) passing the electrode, which was calculated based on the integration of the curve I (A) versus t (s), $\Delta[NH_3]$ and $\Delta[C_{NO_3^-}]$ is the concentration difference of NH_3 and NO_3^- before and after the operation of this electrochemical flow cell.

The partial current density toward ammonia production (j_{NH_3}) is the product of FE for NH_3 production and the applied current density (I_{Total}) as shown in Equation (6)

$$j_{NH_3} = \mathrm{FE}(\%) \times I_{Total} \quad (6)$$

The NH_3 yield rate (mg N h^{-1} mg^{-1}) was obtained by Equation (7)

$$\mathrm{Yield}_{NH_3} = \frac{m_{NH_3}}{t \times m_{CuO}} \quad (7)$$

where m_{NH_3} is the mass of produced NH_3-N (mg), t is the reaction time (h), and m_{CuO} is the mass of coated CuO on the GDE electrode (mg).

The NH_3 recovery efficiency (%) was calculated by Equation (8):

$$NH_3\ \mathrm{recovery}(\%) = \frac{NH_3\ \text{in trap chamber}}{\text{Total generated } NH_3} \times 100 \quad (8)$$

The kinetic constant for NO_3^- reduction (k_{obs}) (h^{-1}) was calculated by a first-pseudo order dependence on nitrate concentration (Equation (9))

$$-\frac{dC_{NO_3^-}}{dt} = k_{obs} C_{NO_3^-} \quad (9)$$

where C_{NO3^-} is the nitrate concentration ($\times 10^{-3}$ M) and t is reaction time (h^{-1}).

Supporting Information

Supporting Information is available from the Wiley Online Library or from the author.

Acknowledgements

The study was financially supported by the NSF PFI-TT project (Award number: 2016472) and the NSF/BSF project (Award number: 2215387). The authors also acknowledge the support of The Brook Byers Institute for Sustainable Systems, Hightower Chair, and the Georgia Research

Alliance at the Georgia Institute of Technology. The views and ideas expressed herein are solely those of the authors and do not represent the ideas of the funding agencies in any form.

Conflict of Interest

The authors declare no conflict of interest.

Author Contributions

J.G. designed/performed the experiment and wrote original draft. Q.M. and J.Y. conducted the DFT and AIMD calculations and AFM/SECM measurement. W.Z. and J.C. were responsible for supervision, conceptualization, writing, reviewing, and editing.

Data Availability Statement

The data that support the findings of this study are available from the corresponding author upon reasonable request.

Keywords

catalyst layer, electron-transfer processes, microenvironments, nitrate reduction, phase-transfer processes, separation science

Received: November 15, 2022
Revised: December 18, 2022
Published online:

[1] a) G. Chen Jingguang, M. Crooks Richard, C. Seefeldt Lance, L. Bren Kara, R. M. Bullock, Y. Darensbourg Marcetta, L. Holland Patrick, B. Hoffman, J. Janik Michael, K. Jones Anne, G. Kanatzidis Mercouri, P. King, M. Lancaster Kyle, V. Lymar Sergei, P. Pfromm, F. Schneider William, R. Schrock Richard, *Science* **2018**, *360*, eaar6611; b) B. H. R. Suryanto, H.-L. Du, D. Wang, J. Chen, A. N. Simonov, D. R. MacFarlane, *Nat. Catal.* **2019**, *2*, 290; c) D. R. MacFarlane, P. V. Cherepanov, J. Choi, B. H. R. Suryanto, R. Y. Hodgetts, J. M. Bakker, F. M. Ferrero Vallana, A. N. Simonov, *Joule* **2020**, *4*, 1186; d) C. Tang, Y. Zheng, M. Jaroniec, S.-Z. Qiao, *Angew. Chem., Int. Ed.* **2021**, *60*, 19572; e) B. Yang, W. Ding, H. Zhang, S. Zhang, *Energy Environ. Sci.* **2021**, *14*, 672.

[2] S. L. Foster, S. I. P. Bakovic, R. D. Duda, S. Maheshwari, R. D. Milton, S. D. Minteer, M. J. Janik, J. N. Renner, L. F. Greenlee, *Nat. Catal.* **2018**, *1*, 490.

[3] a) F.-Y. Chen, Z.-Y. Wu, S. Gupta, D. J. Rivera, S. V. Lambeets, S. Pecaut, J. Y. T. Kim, P. Zhu, Y. Z. Finfrock, D. M. Meira, G. King, G. Gao, W. Xu, D. A. Cullen, H. Zhou, Y. Han, D. E. Perea, C. L. Muhich, H. Wang, *Nat. Nanotechnol.* **2022**, *17*, 759; b) Y. Ren, C. Yu, L. Wang, X. Tan, Z. Wang, Q. Wei, Y. Zhang, J. Qiu, *J. Am. Chem. Soc.* **2022**, *144*, 10193.

[4] a) G.-F. Chen, X. Cao, S. Wu, X. Zeng, L.-X. Ding, M. Zhu, H. Wang, *J. Am. Chem. Soc.* **2017**, *139*, 9771; b) N. Lazouski, M. Chung, K. Williams, M. L. Gala, K. Manthiram, *Nat. Catal.* **2020**, *3*, 463.

[5] a) J. Li, G. Zhan, J. Yang, F. Quan, C. Mao, Y. Liu, B. Wang, F. Lei, L. Li, A. W. M. Chan, L. Xu, Y. Shi, Y. Du, W. Hao, P. K. Wong, J. Wang, S.-X. Dou, L. Zhang, J. C. Yu, *J. Am. Chem. Soc.* **2020**, *142*, 7036; b) G.-F. Chen, Y. Yuan, H. Jiang, S.-Y. Ren, L.-X. Ding, L. Ma, T. Wu, J. Lu, H. Wang, *Nat. Energy* **2020**, *5*, 605.

[6] a) Y. Wang, A. Xu, Z. Wang, L. Huang, J. Li, F. Li, J. Wicks, M. Luo, D.-H. Nam, C.-S. Tan, Y. Ding, J. Wu, Y. Lum, C.-T. Dinh, D. Sinton, G. Zheng, E. H. Sargent, *J. Am. Chem. Soc.* **2020**, *142*, 5702; b) W. He, J. Zhang, S. Dieckhöfer, S. Varhade, A. C. Brix, A. Lielpetere, S. Seisel, J. R. C. Junqueira, W. Schuhmann, *Nat. Commun.* **2022**, *13*, 1129.

[7] a) Y. Wang, W. Zhou, R. Jia, Y. Yu, B. Zhang, *Angew. Chem., Int. Ed.* **2020**, *59*, 5350; b) R. Jia, Y. Wang, C. Wang, Y. Ling, Y. Yu, B. Zhang, *ACS Catal.* **2020**, *10*, 3533; c) Y. Zhang, X. Chen, W. Wang, L. Yin, J. C. Crittenden, *Appl. Catal. B* **2022**, *310*, 121346; d) Z.-Y. Wu, M. Karamad, X. Yong, Q. Huang, D. A. Cullen, P. Zhu, C. Xia, Q. Xiao, M. Shakouri, F.-Y. Chen, J. Y. Kim, Y. Xia, K. Heck, Y. Hu, M. S. Wong, Q. Li, I. Gates, S. Siahrostami, H. Wang, *Nat. Commun.* **2021**, *12*, 2870.

[8] a) W.-J. Sun, H.-Q. Ji, L.-X. Li, H.-Y. Zhang, Z.-K. Wang, J.-H. He, J.-M. Lu, *Angew. Chem., Int. Ed.* **2021**, *60*, 22933; b) R. Daiyan, T. Tran-Phu, P. Kumar, K. Iputera, Z. Tong, J. Leverett, M. H. A. Khan, A. Asghar Esmailpour, A. Jalili, M. Lim, A. Tricoli, R.-S. Liu, X. Lu, E. Lovell, R. Amal, *Energy Environ. Sci.* **2021**, *14*, 3588; c) P. Li, Z. Jin, Z. Fang, G. Yu, *Energy Environ. Sci.* **2021**, *14*, 3522; d) J. Gao, B. Jiang, C. Ni, Y. Qi, X. Bi, *Chem. Eng. J.* **2020**, *382*, 123034; e) J. Gao, B. Jiang, C. Ni, Y. Qi, Y. Zhang, N. Oturan, M. A. Oturan, *Appl. Catal., B* **2019**, *254*, 391.

[9] H. Xu, Y. Ma, J. Chen, W.-x. Zhang, J. Yang, *Chem. Soc. Rev.* **2022**, *51*, 2710.

[10] a) J. Gao, N. Shi, X. Guo, Y. Li, X. Bi, Y. Qi, J. Guan, B. Jiang, *Environ. Sci. Technol.* **2021**, *55*, 10684; b) J. Gao, N. Shi, Y. Li, B. Jiang, T. Marhaba, W. Zhang, *Environ. Sci. Technol.* **2022**, *56*, 11602.

[11] A. Angulo, P. van der Linde, H. Gardeniers, M. Modestino, D. F. Rivas, *Joule* **2020**, *4*, 555.

[12] T. Möller, T. N. Thanh, X. Wang, W. Ju, Z. Jovanov, P. Strasser, *Energy Environ. Sci.* **2021**, *14*, 5995.

[13] a) J. Wicks, M. L. Jue, V. A. Beck, J. S. Oakdale, N. A. Dudukovic, A. L. Clemens, S. Liang, M. E. Ellis, G. Lee, S. E. Baker, E. B. Duoss, E. H. Sargent, *Adv. Mater.* **2021**, *33*, 2003855; b) S.-Q. Liu, E. Shahini, M.-R. Gao, L. Gong, P.-F. Sui, T. Tang, H. Zeng, J.-L. Luo, *ACS Nano* **2021**, *15*, 17757; c) C. Ampelli, *Nat. Catal.* **2020**, *3*, 420; d) H. Rabiee, L. Ge, X. Zhang, S. Hu, M. Li, Z. Yuan, *Energy Environ. Sci.* **2021**, *14*, 1959.

[14] D. Hou, D. Jassby, R. Nerenberg, Z. J. Ren, *Environ. Sci. Technol.* **2019**, *53*, 11618.

[15] A. E. Ketola, W. Xiang, T. Hjelt, H. Pajari, T. Tammelin, O. J. Rojas, J. A. Ketoja, *Langmuir* **2020**, *36*, 7296.

[16] Y. A. Perez Sirkin, E. D. Gadea, D. A. Scherlis, V. Molinero, *J. Am. Chem. Soc.* **2019**, *141*, 10801.

[17] Z. Lyu, S. Zhu, M. Xie, Y. Zhang, Z. Chen, R. Chen, M. Tian, M. Chi, M. Shao, Y. Xia, *Angew. Chem., Int. Ed.* **2021**, *60*, 1909.

[18] J. Kim, W. Choi, J. W. Park, C. Kim, M. Kim, H. Song, *J. Am. Chem. Soc.* **2019**, *141*, 6986.

[19] S. Zheng, Q. Tu, J. J. Urban, S. Li, B. Mi, *ACS Nano* **2017**, *11*, 6440.

[20] D. Wakerley, S. Lamaison, F. Ozanam, N. Menguy, D. Mercier, P. Marcus, M. Fontecave, V. Mougel, *Nat. Mater.* **2019**, *18*, 1222.

[21] a) Z.-Z. Niu, F.-Y. Gao, X.-L. Zhang, P.-P. Yang, R. Liu, L.-P. Chi, Z.-Z. Wu, S. Qin, X. Yu, M.-R. Gao, *J. Am. Chem. Soc.* **2021**, *143*, 8011; b) Z. Xing, X. Hu, X. Feng, *ACS Energy Lett.* **2021**, *6*, 1694.

[22] R. Mao, C. Huang, X. Zhao, M. Ma, J. Qu, *Appl. Catal., B* **2019**, *241*, 120.

[23] Z. Zhu, L. Zhong, T. Horseman, Z. Liu, G. Zeng, Z. Li, S. Lin, W. Wang, *J. Membr. Sci.* **2021**, *620*, 118768.

[24] X. Yuan, S. Chen, D. Cheng, L. Li, W. Zhu, D. Zhong, Z.-J. Zhao, J. Li, T. Wang, J. Gong, *Angew. Chem., Int. Ed.* **2021**, *60*, 15344.

[25] K. Endo, S. Shimada, N. Kato, T. Ida, *J. Mol. Struct.* **2016**, *1122*, 341.

[26] C. Paolucci, A. A. Parekh, I. Khurana, J. R. Di Iorio, H. Li, J. D. Albarracin Caballero, A. J. Shih, T. Anggara, W. N. Delgass, J. T. Miller, *J. Am. Chem. Soc.* **2016**, *138*, 6028.
[27] Y. Xu, J. P. Edwards, J. Zhong, C. P. O'Brien, C. M. Gabardo, C. McCallum, J. Li, C.-T. Dinh, E. H. Sargent, D. Sinton, *Energy Environ. Sci.* **2020**, *13*, 554.
[28] Z. Xing, L. Hu, D. S. Ripatti, X. Hu, X. Feng, *Nat. Commun.* **2021**, *12*, 136.
[29] Y. Wang, Y. Li, J. Liu, C. Dong, C. Xiao, L. Cheng, H. Jiang, H. Jiang, C. Li, *Angew. Chem., Int. Ed. Engl.* **2021**, *133*, 7759.
[30] S. Nayak, B. P. Chaplin, *Electrochim. Acta* **2018**, *263*, 299.
[31] X. Shi, Q. Ma, T. Marhaba, W. Zhang, *J. Visualized Exp.* **2021**, *168*, e61111.
[32] Y. Guo, T. Wang, Q. Yang, X. Li, H. Li, Y. Wang, T. Jiao, Z. Huang, B. Dong, W. Zhang, J. Fan, C. Zhi, *ACS Nano* **2020**, *14*, 9089.